Nanoscale

PAPER

View Article Online
View Journal | View Issue

Cite this: *Nanoscale*, 2022, **14**, 12638

Facilitated transport membrane with functionalized ionic liquid carriers for CO_2/N_2, CO_2/O_2, and CO_2/air separations†

Yun-Yang Lee,[a] Nalinda P. Wickramasinghe,[b] Ruth Dikki,[a] Darrell L. Jan[c] and Burcu Gurkan *[a]

Received 10th June 2022,
Accepted 23rd August 2022

DOI: 10.1039/d2nr03214g

rsc.li/nanoscale

CO_2 separations from cabin air and the atmospheric air are challenged by the very low partial pressures of CO_2. In this study, a facilitated transport membrane (FTM) is developed to separate CO_2 from air using functionalized ionic liquid (IL) and poly(ionic liquid) (PIL) carriers. A highly permeable bicontinuous structured poly(ethersulfone)/poly(ethylene terephthalate) (*b*PES/PET) substrate is used to support the PIL–IL impregnated graphene oxide thin film. The CO_2 separation performance was tested under a mixture feed of $CO_2/N_2/O_2/H_2O$. Under 410 ppm of CO_2 at 1 atm feed gas, CO_2 permanence of 3923 GPU, and CO_2/N_2 and CO_2/O_2 selectivities of 1200 and 300, respectively, are achieved with helium sweeping on the permeate side. For increased transmembrane pressure (>0 atm), a thicker PIL–IL/GO layer was shown to provide mechanical strength and prevent leaching of the mobile carrier. CO_2 binding to the carriers, ion diffusivities, and the glass transition temperature of the PIL–IL gels were examined to determine the membrane composition and rationalize the superior separation performance obtained. This report represents the first FTM study with PIL–IL carriers for CO_2 separation from air.

Introduction

Removal of metabolically generated carbon dioxide (CO_2) from cabin air in spacecraft (2500 ppm CO_2)[1] is accomplished by sorbents like zeolites[1,2] which have high CO_2 capacities. However, zeolites, similar to most common metal organic frameworks,[3] are not selective to CO_2 especially in the presence of moisture and their generation requires significant thermal energy. Furthermore, the temperature swing between room temperature and 300–350 °C creates cracks in the zeolite pellets and dusting.[4] The dusting is problematic because it can migrate to small passages, where it can lodge and cause clogging. This is of particular concern in spacecraft since the dust migration in microgravity will be different from what can be observed in ground tests. Therefore, it is desired to develop new sorbents and less energy demanding separation technologies. Similarly, CO_2 capture from the atmospheric air, referred as direct air capture (DAC), relies on the selective capture of CO_2 from a very dilute concentration (410 ppm CO_2) and sequestration of the captured CO_2 in order to achieve negative emissions. While carbon capture and sequestration is more efficient to implement at point sources of CO_2 emissions, such as power plants, petroleum refinery, and chemical plants where CO_2 concentration is higher, there is still a considerable amount of CO_2 being emitted from discrete sources that are difficult to decarbonize such as transportation (29%), commercial and residential buildings (13%), and agricultural activities (10%) that total up to 52% of the overall CO_2 emissions.[5] Therefore, carbon negative technologies such as DAC are essential to stay below the projected 1.5 °C temperature rise globally.[6]

Simple thermodynamical calculations (see ESI†) suggest that the theoretical minimum work for DAC, where CO_2 is 410–420 ppm, is almost four times greater than that from post-combustion CO_2 capture (PCCC) where the CO_2 is about 20%. Accounting for the fluid transportation, compression, heating, and thermal exchange, the overall energy demand for CO_2 separation from dilute stream (*e.g.*, 410–2500 ppm) is much greater than the theoretical work. The estimated energy

---

[a] *Department of Chemical and Biomolecular Engineering, Case Western Reserve University, Cleveland, OH 44106, USA. E-mail: yxl2286@case.edu, beg23@case.edu, rcd82@case.edu*

[b] *Northeast Ohio High Field NMR Facility, Case Western Reserve University, Cleveland, OH 44106, USA. E-mail: npw8@case.edu*

[c] *Ames Research Center, National Aeronautics and Space Administration, Moffett Field, CA 94043, USA. E-mail: darrell.l.jan@nasa.gov*

† Electronic supplementary information (ESI) available: NMR characterization of IL, PIL, and GO; pulse sequence and the spectra recoded for ^{1}H-DOSY NMR; viscosity and water content of IL as a function of CO_2 concentration and humidity; FTIR, SEM, and photo images of the membranes; details of the transport model fit; membrane specifications for the tested vacuum operation. See DOI: **https://doi.org/10.1039/d2nr03214g**

requirement for DAC (410 ppm) and space cabin air (2500 ppm) is in the range of 200 to 400 kJ per mol CO_2,[7–10] whereas the energy for PCCC is roughly half of that.[10] The state-of-the-art DAC technologies, with a few demonstrations in pilot scale,[11] rely on either the solid adsorption or liquid absorption of CO_2. Liquid systems pass air through solutions like aqueous amines[12] or alkali metal hydroxides.[13,14] Solid systems utilize supported amine sorbents[15–17] and humidity-swing quaternary ammonium based anion-exchange resins.[18,19] However, these sorption techniques are energy-intensive processes, since the strong binding of amine and CO_2 (C–N bond, about −80 kJ mol^{-1})[20] requires a temperature of around 120 °C to cleave off CO_2 for sorbent regeneration. Similarly, the calcination temperature of above 700 °C for alkali/alkaline earth carbonates[21] results in a high energy demand.

In contrast to absorption and adsorption technologies, membrane separation is a non-equilibrium process that operates by mass control[22] and under isothermal conditions with typically higher energy efficiency. It is also a promising technology for its high modularity, process simplicity, and lower operational cost.[23] Conventional solution–diffusion (S–D) gas separation membranes rely on the difference in solubility and diffusivity of the target gas over other gas components for separation.[24] Recent progresses on the S–D membranes focused on increasing (1) the solubility selectivity toward CO_2 over other gases by the incorporation of highly polar or ionic components;[25–29] and (2) the diffusivity selectivity for CO_2 sieving by rigid polymeric backbones with high free volume.[30–34] There is usually a tradeoff between gas permeance and selectivity of a membrane, as described by the Robeson upper-bound.[35–37] The S–D type membranes are often implemented as multi-stage membrane systems to achieve the desired separation, which inevitably drives up the energy consumption. Facilitated transport membranes (FTMs) utilize CO_2-philic carriers such as amines that chemically bind with CO_2, thus enabling CO_2 transport by both (1) vehicular motions (CO_2 transport in the form of CO_2-carrier complexes) and (2) hopping motions (CO_2 transport *via* hopping along a number of CO_2-philic sites) of the carriers, along with (3) CO_2 diffusion, following the direction of transmembrane CO_2 gradient.[38] Therefore, the CO_2 permeation is significantly improved even under reduced CO_2 partial pressures while maintaining a high selectivity.[39] Therefore, FTMs perform above the Robeson upper-bound. Amine functionalized polymers are the most common FTMs that are referred as having fixed site carriers. FTMs that incorporate amine-based salts and ionic liquids (ILs) as mobile carriers[40–47] are shown to further enhance CO_2 transport.[48]

While FTMs have been studied for CO_2 separation from post-combustion flue gas, there are only a few reports that we are aware of discussing their utility relevant for DAC and for CO_2 removal from cabin air.[49–51] Under DAC and cabin air conditions, there is very small driving force for CO_2 transport owing to low concentration, temperature, and humidity; hence, it is extremely challenging to concentrate the CO_2 on the effluent side. There has been two reports assessing membrane-based DAC processes by simulations based on (1) a hypothetical non-FTM[52] with ultra-high permeance (40 000 GPU) and low CO_2/N_2 selectivity (70); and (2) a hypothetical FTM[53] with high permeance (2500 GPU) and high CO_2/N_2 selectivity (680). In 2022, Sandru *et al.* fabricated a three-layered composite membrane with an ultrathin surface-grown amine-rich top layer (10 nm) and a thin mid-layer of highly permeable amorphous polytetrafluoroethylene, PTFE, (1 μm) coated over a porous membrane support as the bottom layer (50 μm).[54] The fabricated membrane achieved a CO_2 permeability of 1000 Barrer (equivalent to 50 000 GPU; calculated based on the reported overall membrane thickness of 50 μm) and a CO_2/N_2 selectivity greater than 1000, with a CO_2/N_2 feed (10/90, v/v; RH = 100%) at 25 °C. The authors observed no diffusion limitations, unlike the previously reported thicker polyallylamine FTM (1 μm in thickness; 300 GPU and selectivity of 23).[55] While this membrane was not tested under conditions relevant to DAC or cabin air, it demonstrates the importance of a thin selective layer and a highly permeable substrate to overcome the selectivity–permeability trade-off.

Lee and Gurkan reported a poly(ionic liquid)–ionic liquid/graphene oxide (PIL–IL/GO) composite membrane in 2021 as the first representative FTM specifically designed for CO_2/N_2 separation relevant to DAC and CO_2 removal from cabin air.[56] The PIL–IL carriers were nanoconfined within the GO nano framework (GONF) resulting in a 900 nm-thick CO_2 selective layer on an ultrafiltration (UF) membrane substrate. The choice of the mobile carrier, 1-methyl-3-ethylimidazolium 2-cyanopyrrolide, [EMIM][2-CNpyr], enabled the reactivity–mobility balance of CO_2 by synergizing the IL's high affinity to CO_2 and low viscosity (in comparisons to other reactive ILs). A high CO_2 permeance of 3090 GPU coupled with a high CO_2/N_2 selectivity of 1180 was demonstrated by the PIL–IL/GO FTM under 410 ppm CO_2 feed at 25 °C and 40% RH. This performance is superior to other known polyvinylamine and PIL ionomer based FTMs under similar conditions.[40,47] Here, we extend this work and report a thin PIL–IL/GO selective layer on a *b*PES/PET substrate with well-interconnected pores as highly permeable FTM that demonstrates high performance of CO_2 separation from $CO_2/N_2/O_2/H_2O$ mixture at extremely low CO_2 partial pressures. The impacts of oxygen and water on CO_2 capacity and the diffusivity of the carrier were examined by ^{13}C-NMR and ^{1}H-DOSY NMR. The specific interactions between the GONF and the PIL–IL gel was characterized by HSBC NMR and FTIR. This study reports on the CO_2/O_2 selectivity and tunability of the $CO_2/(N_2 + O_2)$ separation ratio, and the mechanical strength against a transmembrane pressure for PIL–IL/GO type FTMs through the modifications of the PIL–IL composition and GONF layer thickness.

Experimental section

Materials

The IL precursor, 1-ethyl-3-methylimidazolium iodide ([EMIM][I], >98%) was purchased from TCI America. The ACS grade reagent methanol, isopropanol, and acetone were purchased from Alfa Aesar *via* Thermo Scientific. Anion precursor pyrrole-2-carbonitrile (99%) and Amberlite® IRN-78 anion exchange resin (AER) in [OH^-] form were purchased from Thermo Scientific. The poly(ionic liquid) (PIL) precursor, poly (diallydimethylammonium chloride) (P[DADMA][Cl], M_w 400–500 kDa, ∼20 wt% aqueous solution) and paramagnetic compound chromium acetylacetonate ($Cr(ACAC)_3$, 97%) were purchased from Millipore-Sigma. The AER was washed with methanol for at least three times and vacuum dried at room temperature before use. Solid P[DADMA][Cl] was acquired by directly pulling vacuum on the aqueous solution at 40 °C for three days and 80 °C for a day. The deuterated solvent DMSO-d_6 (25 ml, 99.8%) was purchased from Thermo Scientific. The NMR tubes (5 mm OD; 7″ L; wall thickness: 0.38 mm) with coded closed caps were purchased from Bruker. The NMR coaxial tube set (inner cell: NE-5-CIC; outer cell: NE-UPE-7) were purchased from New Era Enterprises, Inc.

The ultrafiltration (UF) substrate membrane (LY; nominal cutoff of 100 kDa) with poly(ethersulfone) (PES) skin layer and poly(ethylene terephthalate) (PET) nonwoven substrate was purchased from Synder Filtration. The *b*PES/PET was prepared following the procedure as described by Pang *et al.*[57] Briefly, the highly gas permeable substrates with bicontinuous structured skin layer (with pore size of 30–40 nm) were fabricated by water-vapor induced phase separation, followed with water immersion. This highly permeable membrane is abbreviated as *b*PES/PET to make a distinction from the commercial UF substrate. Single-layer graphene oxide (GO) dispersion (5 mg ml^{-1}) was purchased from ACS Material (synthesized by modified Hummers' method and have an average width and thickness of 0.3 μm and 0.8 nm, respectively).

Tank gases of nitrogen (N_2; Ultra High Purity (UHP)), argon (Ar; UHP), helium (He; UHP), carbon dioxide (CO_2; bone dry), hydrogen (H_2; UHP), and synthetic air (synthetic blend of N_2 (80%) and O_2 (20%), with less than 1 ppm of CO_2) were purchased from Airgas.

Methods

Synthesis of [EMIM][2-CNpyr] (IL) and P[DADMA][2-CNpyr] (PIL). The synthesis of IL and PIL started with the anion exchange step of the precursor materials of [EMIM][I] (10 g in 100 ml methanol) and P[DADMA][Cl] (10 g in 100 ml methanol), respectively, into OH^- intermediates. The use of AER to precursor was monitored to be around 5 mg AER per mmole precursor. The residual halide content in the intermediate solution was tested by 0.1 N silver nitrate ($AgNO_3$) solution and confirmed to be low (<1000 ppm) from the lack of visual white precipitates of silver halides. The halide contents were further determined to be lower than 0.25% (detection limit) by combustion ion chromatography. The intermediate solutions of IL and PIL in $[OH]^-$ form were separately mixed with the anion precursor pyrrole 2-carbonitrile (with cation to anion precursor molar ratio of 1 : 1.02 mol) for acid–base neutralization reaction to complete overnight. The excess solvent was removed from the resulting solutions by rotary evaporation at 60 °C. Samples were then vacuum dried at 80 °C for overnight to remove residual water. The molecular structure of the synthesized PIL and IL were characterized and confirmed by ^1H-NMR and heteronuclear single quantum coherence (HSQC), heteronuclear multiple bond correlation (HMBC) on a Bruker 500 MHz (Fig. S1 and S2†).

Fabrication of PIL–IL/GO composite membrane

Both UF and *b*PES/PET membrane substrates were rinsed with methanol/DI water (1 : 1, v/v) for at least three times to remove residual salt crystals from the substrate. This step is important as these contaminants can change the surface charge of GO flakes in the suspension in the next step, causing coagulation and failure of the GONF layer deposition. The membranes were dried in vacuum at 40 °C overnight prior to use. The GO in water dispersion (0.2 mg ml^{-1} and 2 mg ml^{-1}) were prepared by diluting the purchased GO solution (5 mg ml^{-1}) with DI water and sonication. The GONF layer was deposited over the substrates by vacuum filtering the GO suspension on top of the membrane substrate (with level accuracy checked) for roughly 5–10 min. To ensure even coverage and a final GONFL layer with homogenous thickness, the leveling of the membrane was confirmed to be perfectly horizontal. The deposited GONF layer was then impregnated by the PIL–IL gel by drop casting. The PIL–IL casting solution was prepared by mixing 0.2 mg ml^{-1} of PIL and 20 mg ml^{-1} of IL in methanol. The fabricated PIL–IL/GO on *b*PES/PET membranes were allowed to dry under ambient air and were kept under vacuum at ambient temperature before use.

Materials characterization

The Fourier-Transformed Infrared (FTIR) spectra of the IL, PIL, and membranes were taken on Nicolet iS50 (Thermo Scientific) using a diamond crystal attenuated total reflectance (ATR) unit. Water content of the ILs were confirmed to be <1000 ppm by a coulometric Karl Fischer titrator (Metrohm; 889D). Viscosity of the IL was measured with a viscometer (RheoSense; microVisc) equipped with microchannel chips (Rheosense A05, A10, and B20). The phase transition of PIL–IL gels was performed with a DSC (Mettler Toledo DSC3), where the PIL–IL gels (∼15 mg) were pre-loaded into Al pans and sealed in Ar atmosphere glovebox (VTI; H_2O and O_2 < 0.1 ppm). The sample pans were first held at 80 °C (5 min), then cooled to −90 °C and held for 50 min, and finally heated back to 80 °C with a rate of 10 °C min^{-1} under N_2 for three cycles. No differences were observed among the cycles and therefore only the glass transition temperature (T_g) of the third cycle is reported. The surface morphology and cross-sectional topography of the membranes were taken by field emission scanning electron microscopy (FESEM; ThermoFisher Apreo 2S). All membrane samples were sputtered with about 5 nm Pd prior to analysis for high conductivity and better image resolution.

CO_2 binding capacity

The $CO_2/N_2/O_2$ gas mixture was prepared by mixing the CO_2 with the as-purchased synthetic air (N_2/O_2) by mass flow controllers (MFCs; Brooks 5850i) with Labview® *via* data acquisition units (DAQ; National Instrument 782604-01). The humidity control was achieved by a water bubbler. For the precise control of temperature, the gas lines, including the water bubbler, was kept inside an incubator (HettCube 400R; Across International LLC). The mixing of the gases for the desired compositions of 410, 1000, 2500, 5000, 10 000, and 20 000 ppm of CO_2 at 22 °C and 40% relative humidity level (40% RH at 22 °C refers to 7.9 Torr or 10.6 mbar) was done in a 300 mL metal chamber (Swagelok) within the incubator. The gas flow rate was measured by ADM 2000 Flowmeter (J&W Scientific Inc., acquired by Agilent). A CO_2 analyzer (SBA-5, PPSystems Inc.) with a detection range of 0 to 20 000 ppm was used to confirm the CO_2 concentration in the prepared gas mixtures. To determine the CO_2 absorption capacity of the IL, the gas mixture with the set CO_2 content (200 ml min^{-1}) was contacted with the IL (1 g) under 60 rpm agitation in a glass vial (20 ml) for at least 6 h at 22 °C for equilibrium. The equilibrium for CO_2 saturation was reached within 2–3 h, whereas the equilibrium for the set relative humidity took longer. Therefore, a wait time of 6 h was allowed to ensure the system reached thermodynamic equilibrium. The binding capacity between CO_2 and IL carrier was studied by quantitative ^{13}C-NMR. Following CO_2 absorption, 20 mg of the IL was sampled into 0.6 ml of 0.1 M $Cr(ACAC)_3$ DMSO-d_6 solvent and quantification of the CO_2–IL complex followed the previously reported method.[58] The identified products were identical to our previous report;[58] briefly the peaks at 146, 154, and 158 ppm were assigned to carbamate, carboxylate, and bicarbonate complexes, respectively.

Self-ion diffusivities

Self-diffusion coefficient of the IL was measured by Diffusion-Ordered Spectroscopy (DOSY) on the same 500 MHz NMR. About 0.3 ml of DMSO-d_6 was loaded into the inner cell and the top was flame sealed (or sealed with epoxy resin). About 1.5 ml of the CO_2-saturated IL (at 410, 1000, 2500, 5000, 10 000, and 20 000 ppm CO_2 under 40% RH) was transferred into the outer cell and the atmosphere in the headspace was purged with the same atmosphere used for CO_2 absorption. The inner cell was then inserted into the outer cell and sealed with coded close cap and parafilm to ensure a gas tight environment. The samples were measured using bipolar gradient pulse sequence (ledbpg2s) and the *Z*-gradient diffusion probe (Fig. S3a†). The diffusion times (Δ) and gradient pulse duration (δ) were optimized in subsequent experiments according to practical needs, until full exponential decay pattern of magnetization was observed within 16 pulse gradient strengths (from 2% to 98%) (Fig. S3b and S4a†). The isotopic self-diffusivity (D) of ions was calculated using eqn (1) *via* MestReNova.

$$M(g) = M_0 e^{\left[-(\gamma g \delta)^2 D\left(\Delta - \frac{\delta}{3}\right)\right]} \tag{1}$$

where γ is the gyromagnetic ratio, g is the magnitude of the gradient pulse, δ is the duration of the gradient pulse, and Δ is the interval (drifting or diffusion time) between two gradient pulses in the opposite direction. M_0 is the strength of magnetization without pulse field gradient applied, whereas $M(g)$ is the measured magnetization that exponentially decay as a function of applied pulse field gradient strength. An example of the calculated ^{1}H-DOSY is shown in Fig. S4b.†

Membrane tests

The gas separation performance of the PIL–IL/GO composite membrane was tested under both sweep and vacuum modes. The membrane was placed in between two aluminum foils and fastened in a stainless-steel permeation cell (Advantec). The membrane module along with the bubbler and gas mixing chamber were kept within the temperature and humidity-controlled incubator (HettCube 400R; Across International LLC). Simulated $CO_2/N_2/O_2/H_2O$ feed gas of 410, 1000, 2500, 5000, and 10 000 ppm CO_2 with various humidity level were prepared by fine tuning the gas flow rate of the anhydrous CO_2, anhydrous synthetic air (N_2/O_2 = 80/20), and moisture saturation by passing the specific gas streams through the water bubbler. The $CO_2/N_2/H_2O$ feed gas were prepared by mixing anhydrous CO_2, anhydrous N_2, and moisture saturated N_2. Fig. 1 shows the schematic of the membrane testing setup. The permeate side of the membrane module has both the helium sweep (0 Torr gauge pressure; single solid line) and the vacuum (−760 Torr gauge pressure; double solid line) capability for testing of different transmembrane pressures. The flow rate of feed gas and sweep gas were kept constant as 200 cm^3 min^{-1}. For tests under the sweeping mode (labeled with pathway ① in Fig. 1), the permeate gas was carried by the He sweep directly to a gas chromatography, GC (Agilent 7890B) with a micro-packed column and thermal conductivity detector (TCD) with He mobile phase for quantitative compositional analysis. For tests under vacuum operation (labeled with pathway ② in Fig. 1), the permeate was first collected by a pump (Agilent; IDP-7 dry scroll pump) under vacuum and then mixed with the He sweep, as shown, for GC analysis. The specific testing conditions are listed in Table 1.

The gas separation performance was calculated in gas permeance unit (GPU; 1 GPU = 3.348 × 10^{-10} mol m^{-2} s^{-1} Pa^{-1}) by eqn (2).

$$P_i = 10^6 (Q_i / (A \cdot \Delta p_i)) \tag{2}$$

where Q_i is the permeating rate of component i (cm^3 s^{-1}), A is the membrane area (5.06 cm^2), and Δp_i is the transmembrane partial pressure gradient for component i (cmHg). The uncertainty in permeance (P_i) was determined from the propagation of error analysis using the respective uncertainties in A (±0.11 cm^2 based on the measured membrane coupon radius of ±0.2 mm), Δp_i (±0.01 cmHg based on the measured concentrations by GC) and the standard deviation in the repeated measurements for Q_i (varied for each of the conditions in the range of 0.0001–0.0003 cm^3 s^{-1} for 5 measurements).

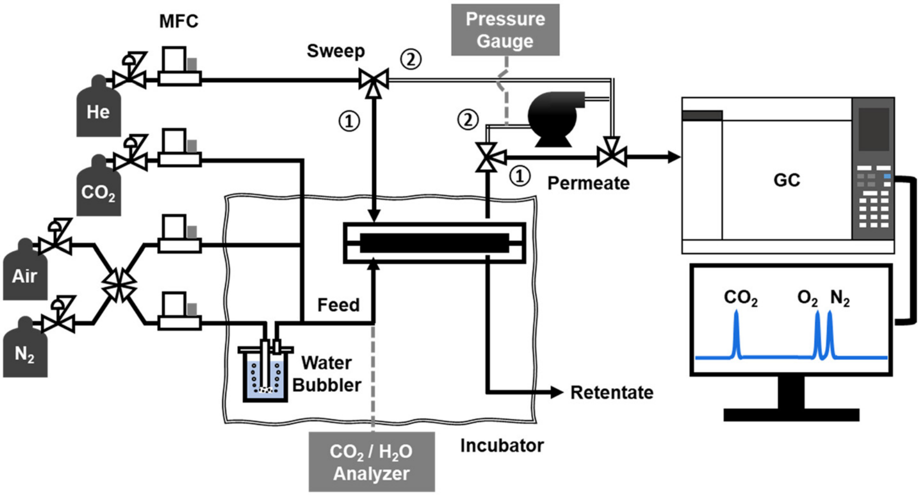

Fig. 1 Schematics of the membrane test unit. Permeate gas was collected and sent to gas chromatogram (GC) either by He sweep (path ①) or by vacuum (path ②) for a transmembrane pressure of 0 or 1 atm, respectively. The balance gas of CO_2 is either synthetic air (N_2/O_2 = 80/20) or N_2 for the $CO_2/N_2/O_2/H_2O$ or $CO_2/N_2/H_2O$ mixtures, respectively.

Table 1 Fabricated FTM specifications and the membrane testing conditions

Membrane substrate					
Membrane #	i	ii	iii	iv	v
Substrate	UF	*b*PES/PET			
Membrane area	5 cm^2				
Selective layer					
PIL–IL/GO (mg–mg/mg)	0.2–20/0.2		0.4–40/0.4	0.5–50/0.5	1.25–3.75/1
Thickness (μm)	0.9		1.4	1.6	2.0
Membrane testing condition					
Feed; sweep	200 cm^3 min^{-1}; 200 cm^3/min				
CO_2 in feed (ppm)	410, 2500, and 10 000 (1%), CO_2 balanced with N_2 or synthetic air (N_2/O_2 = 80/20) at 760 Torr				
Transmembrane pressure (Δ*P*; Torr)	0				760
Temperature (K)	295 and 313 K				
Relative humidity (% RH)	0, 40, and 80				40

The selectivity of CO_2 over N_2 (α_{CO_2/N_2}) and CO_2 over O_2 (α_{CO_2/O_2}) are calculated using eqn (3) and (4), respectively. The separation ratio ($\alpha_{CO_2/(N_2+O_2)}$), which is the permeance ratio of CO_2 over the sum of N_2 and O_2, is a parameter that better describes the performance of gas separation in ternary gas mixtures, and it is calculated using eqn (5).

$$\alpha_{CO_2/N_2} = \frac{P_{CO_2}}{P_{N_2}} \tag{3}$$

$$\alpha_{CO_2/O_2} = \frac{P_{CO_2}}{P_{O_2}} \tag{4}$$

$$\alpha_{CO_2/(N_2+O_2)} = \frac{P_{CO_2}}{P_{N_2} + P_{O_2}} \tag{5}$$

The dependence of CO_2 permeance on the CO_2 partial pressure of the feed is described by a homogenous reactive diffusion model given in eqn (6).[39,47]

$$\frac{P_{CO_2}}{l} = \frac{P^0_{CO_2}}{l}\left[1 + \eta_{CO_2}\left(\sqrt{1 + \frac{p^*_{CO_2}}{p^h_{CO_2}}} - 1\right)\right] \tag{6}$$

where l is the thickness of the membrane, P_{CO_2}/l is the measured CO_2 permeance, $P^0_{CO_2}/l$ is a fit parameter that represent the CO_2 permeance (GPU) at saturation of carriers (corresponding to the CO_2 permeance from S–D pathway), η_{CO_2} is the efficacy of the facilitated transport pathway, $p^*_{CO_2}$ is the partial pressure of CO_2 in the feed when the carriers are saturated with CO_2, and $p^h_{CO_2}$ is the set CO_2 partial pressure in the feed.

Results and discussion

We first present the results from the characterization of the CO_2 carrier, namely the [EMIM][2-CNpyr], in terms of its CO_2 binding capacity in the presence of N_2 and O_2, measurement of ion self-diffusivities, and the thermal behavior of the IL when gelled with PIL. The fabricated membranes with the PIL–IL gel is then described through their topological and cross-sectional features as determined by SEM as well as the specific interactions among the PIL, IL, and GO components examined by FTIR and NMR methods. Finally, the CO_2 separation performance of the FTMs under synthetic air feed and at varying temperature and humidity conditions are presented.

CO_2 binding and transport

CO_2 binding to the IL and the ion diffusivities in the presence of O_2 (16–20%) is studied at 22 °C and 40% RH (10.6 mbar). The CO_2 absorption by [EMIM][2-CNpyr] has been previously shown[56,58] to form carbamate (CO_2 binding to the pyrrole anion), carboxylate (CO_2 binding to the imidazolium cation), and bicarbonate (CO_2 binding to the co-absorbed water) species in both pure CO_2 and CO_2/N_2 mixture gas. The distribution of these products was found to be different at low CO_2 partial pressures in CO_2/N_2 compared to pure CO_2. Fig. 2a shows the breakdown of the measured CO_2 binding capacities, calculated from the ^{13}C-NMR peak integration of carbamate at 146 ppm (–N–COO), carboxylate at 154 ppm, and bicarbonate (HO–COO) with (red bordered) and without O_2 presence (black bordered). At 410 ppm, 40% of the total capacity under pure CO_2 is achieved in both cases of with and without O_2, showing the strong interactions between the IL and CO_2. The capacity at 2500 ppm of CO_2 is about 60% of the total capacity under pure CO_2 (4.3 mole CO_2 per kg sorbent). Within the gas compositions studied, there is no significant influence of O_2 on the measured solubility of CO_2. The physisorbed of CO_2 within the entropic voids of the [EMIM][2-CNpyr] is expected to be less than 3% of the overall CO_2 solubility.[59] The physiosorbed O_2 is expected to be at least a factor lower[60] than that of physiosorbed CO_2 in ILs in general. This is due to the high polarizability of the quadrupolar CO_2 within ionic environments, in contrast to nonpolar O_2. The measured bulk viscosity of the IL is also not influenced much with O_2 (Fig. S5a†). However, as seen in Fig. 2b, the measured ideal diffusivities of the imidazolium cation (filled symbols) and the pyrrolide anion(hollow symbols) demonstrate a weak dependence on O_2 (3–5% difference between gray and red symbols) and a strong dependence on CO_2.

The ion self-diffusivities were measured by ^{1}H-DOSY NMR (Fig. S4†). The diffusivity of imidazolium (D^+) is higher than the pyrrolide (D^-) despite the smaller size of the pyrrolide anion. Previous studies[61,62] on various ILs reported similar observations and attributed this trend to the hydrogen bonding associated mostly with the anions. The diffusivity of [EMIM], [2-CNpyr], and their CO_2-complexes are around 10^{-7} $cm^2\ s^{-1}$ at 22 °C, which is an order of magnitude higher than the reported ion diffusivities for a similar CO_2 reactive IL 1-methyl-3-ethylimidazolium acetate (~10^{-8} $cm^2\ s^{-1}$ with a viscosity of 2700 cP).[63] The CO_2-complexed ions could not be resolved effectively from their parent ions as they appeared as single peak for both the imidazolium and the pyrrolide. This is attributed to the strong H-bonding[58] between the CO_2 complexed and un-complexed ions and the fast exchange of proton between these species. The strong dependence of the ideal diffusivity of both the cation (D^+) and the anion (D^-) on the quantity of CO_2 within the IL is also indicative of the increased intermolecular hydrogen bonding that leads to slower diffusion. It should be noted that the direct deconvolution of different transport mechanism of CO_2 (diffusion, hoping, and vehicular motion) is not possible at this point by ^{1}H-DOSY since CO_2 itself is not proton-bearing. Therefore, the measured diffusivities of ions reflect the overall transport of carrier-CO_2 complex. The (D^+/D^-) ratio remained in the range of 1.18–1.23 for all of the conditions studied, suggesting no major changes in the solvation environment when O_2 is present in the carrier liquid.

The incorporation of PIL into IL provides mechanical reinforcement by forming a non-crosslinked gel. In turn, the IL component acts as the plasticizer for mobility enhancement of the CO_2 carrier. Fig. 3 shows the phase-transition of PIL–IL gels in the bulk as characterized by DSC. The plotted red

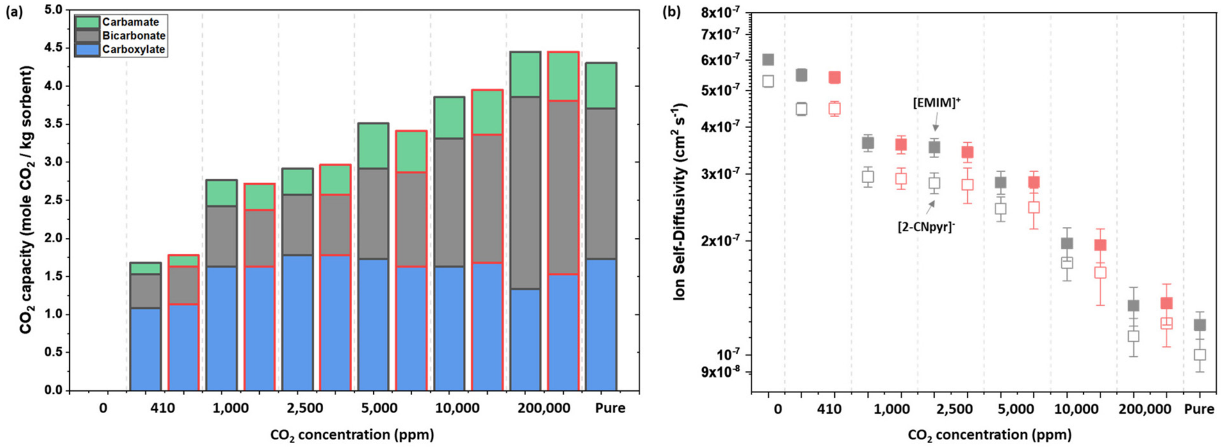

Fig. 2 (a) Measured CO_2 capacity of [EMIM][2-CNpyr] at 22 °C and 40% RH (10.6 mbar) by quantitative ^{13}C-NMR with and without (red bordered bars) O_2 in the synthetic air feed. The O_2 concentration in the gas mixtures was maintained at about 20% with the exception of 200 000 ppm CO_2 where O_2 concentration was 16%. The uncertainty in the reported capacities is calculated from the signal to noise ratio and found to be less than 0.05 mole CO_2 per kg sorbent. (b) The dependence of self-diffusivities of $[EMIM]^+$ (filled symbol) and $[2\text{-}CNpyr]^-$ (hollowed symbol) on the CO_2 concentration in the absorbed feed gas with (red) and without (gray) O_2.

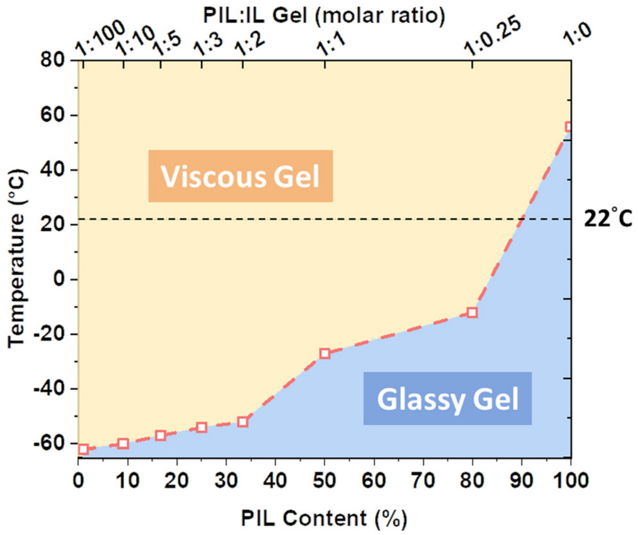

Fig. 3 The phase diagram of PIL : IL mixture (in molar ratio) measured by DSC, with a scanning rate of 10 °C min^{-1} under N_2. The glass transition (T_g) points are connected with red dashed line as the hypothetical trend of phase-transition of the gel from the glassy state to elastomeric state. The plot of DSC curve from which T_g was obtained is given in Fig. S6.†

squares are the glass transition temperatures (T_g) of the PIL–IL gels, as determined from the midpoint of the transition region of the DSC curves. The T_g decreases as the amount of PIL decreases. In order to have a mobile carrier within the membrane at cabin or atmospheric temperatures, it is more desirable to have a viscous gel than a glassy one. Therefore, optimization of the PIL–IL content is necessary for a targeted permeance. Too high of a PIL content would increase the membrane resistance while too high of an IL content may not demonstrate sufficient mechanical stability against large transmembrane pressures. We tested the PIL : IL composition of 1:100, similar to our previous work,[56] to allow for high carrier mobility, for the sweeping mode of operation and the 1 : 3 PIL : IL composition to improve stability of the carrier within the membrane architecture against vacuum mode of operation on the permeate side.

Characterization of PIL–IL/GO membrane

In comparison to the commercial UF membrane substrate (Fig. 4a), the schematics and the SEM images of *b*PES/PET substrate are shown in Fig. 4b. The *b*PES skin layer has an interconnected porous structure with a pore size of roughly 30–40 nm[64] (Fig. 4b, right panel) whereas the UF substrate has a semi-dense PES skin layer (Fig. 4a, right panel). The fabrication of GONF on the *b*PES/PET substrate was done by vacuum filtering where the GO nanosheets (each with about 0.3 µm width) were deposited homogeneously to give a wrinkled top surface (Fig. 4c, right panel). The deposited GONF is estimated to consist of about 250 to 260 GO layers, based on the individual sheet thickness of 0.8 nm and spacing of 1 nm in between the GO layers.[56] The impregnation of the PIL–IL gel into the GONF layer caused swelling and change in surface morphology with a final PIL–IL/GO selective layer thickness of about 850 nm (Fig. 4d) in comparison to GONF thickness of about 450 nm (Fig. 4c).

The specific interactions between GO and PIL–IL gel were probed by FTIR and NMR methods. Fig. 5 shows the FTIR spectra of PIL–IL/GO on *b*PES/PET substrate (ii in Table 1), where the characteristic features of PIL–IL ($\nu_{\text{aromatic-CH}}$ 3100 cm^{-1}, $\nu_{\text{alkyl-CH}}$ 2900 cm^{-1}, and $\nu_{\mathrm{C{\equiv}N}}$ 2220 cm^{-1}) and GO (ν_{OH} 3430 cm^{-1}, $\nu_{\mathrm{C{-}(C{=}O)}}$ 1720 cm^{-1}, and $\nu_{\mathrm{C{=}C}}$ 1570 cm^{-1}) were confirmed. The observation of the red-shifted GO peaks (ν_{OH} 3430 cm^{-1} and $\nu_{\mathrm{C{-}(C{=}O)}}$ 1720 cm^{-1}; highlighted with red arrows) and the blue-shifted PIL–IL peaks ($\nu_{\text{aromatic-CH}}$ 3100 cm^{-1}, $\nu_{\text{alkyl-CH}}$ 2900 cm^{-1}, and $\nu_{\mathrm{C{\equiv}N}}$ 2220 cm^{-1}; highlighted with blue arrows) suggest the molecular interactions between the PIL, IL, and GO components.[65] Fig. S7b† compares the peak shifts of the PIL–IL/GO on UF and *b*PES/PET substrate, in which we don't see much difference in the featured characteristic peaks. Therefore, we concluded that the nano-confinement of PIL–IL in GONF is effective, and the PIL–IL gel is not leached out into the substrate even when the pore size increase from UF (3–4 nm) to *b*PPES/PET (30–40 nm). The photo images of the PIL–IL/GO and GONF on UF and *b*PES/PET substrates are in Fig. S7a.†

The HMBC NMR (Fig. 6a) further provided support to the interactions between the PIL–IL and GO by FTIR by specifically probing the correlated ^{1}H and ^{13}C within the selective layer components. In order to remove the interference from the majority component, which is the substrate, the PIL–IL/GO flakes (Fig. 6a, inset) were scraped from the membrane surface and re-dissolved in DMSO-d$_6$ for HMBC. The correlations between the imidazolium ring (g, i, and k) and GO were highlighted in yellow at the intersections of the dashed lines (Fig. 6a). This interaction between [EMIM]$^+$ and GO is ascribed to both the π–π and electrostatic interactions.[65–67] Moreover, ^{1}H-NMR of PIL–IL/GO also suggests the interaction between PIL–IL and GONF. Fig. 6b compares the ^{1}H-NMR of PIL–IL/GO and PIL–IL gel. With a molar ratio of PIL : IL = 1 : 100, we observed the spectra to be almost the same as IL (Fig. S1a†) since the proton signal of PIL is diminished due to its low concentration (Fig. 6b, bottom). With the confinement of PIL–IL within the GONF, the characteristic peaks of [EMIM]$^+$ cation "a, b, c, g, i, and k" broaden[68] due to the relatively slow movement of the ions within the NMR time scale (Fig. 6b, top). Such broadening effect was observed only in the IL constituent and was not observed on the line width of the d-solvent (DMSO-d$_6$ at 2.58 ppm, labeled with *). The OH moiety of GO component is also downshifted to 4.7 ppm (Fig. 6b, top) from 3.4 ppm that is seen in pure GO sample without the presence of PIL or IL (Fig. S8†). This shift further supports the existence of interactions between the PIL–IL and GO.

CO_2 separation

The CO_2 permeance and CO_2 selectivity against N_2 and O_2 with the PIL–IL/GO FTMs were measured by membrane testing

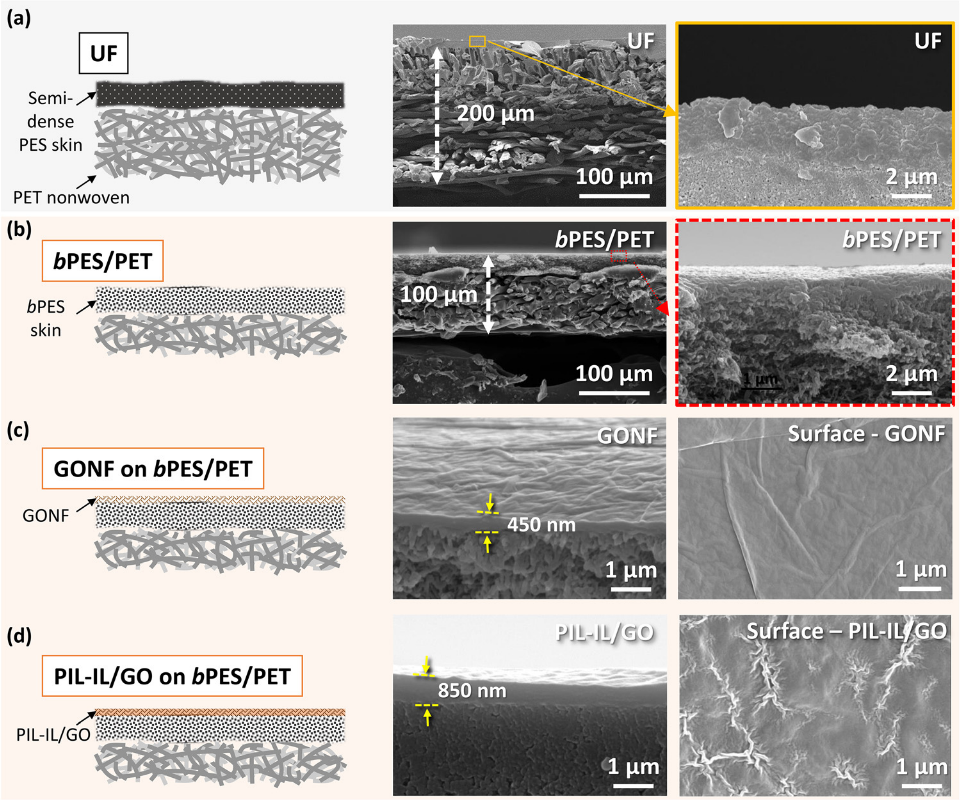

Fig. 4 Schematics and the cross-sectional SEM images of UF substrate (a), the fabricated *b*PES/PET substrate (b), GONF on *b*PES/PET substrate (c), and PIL–IL/GO selective layer on *b*PES/PET substrate (d). The zoomed-in images on the right for (a) and (b) panels show the difference in porosity of the PES skin layer. The surface morphology shown on the right of panels (c) and (d) represent the GONF top surface before and after impregnation with PIL–IL gel, respectively. The surface morphology of the unmodified UF and *b*PES/PET substrates are shown in Fig. S7a.†

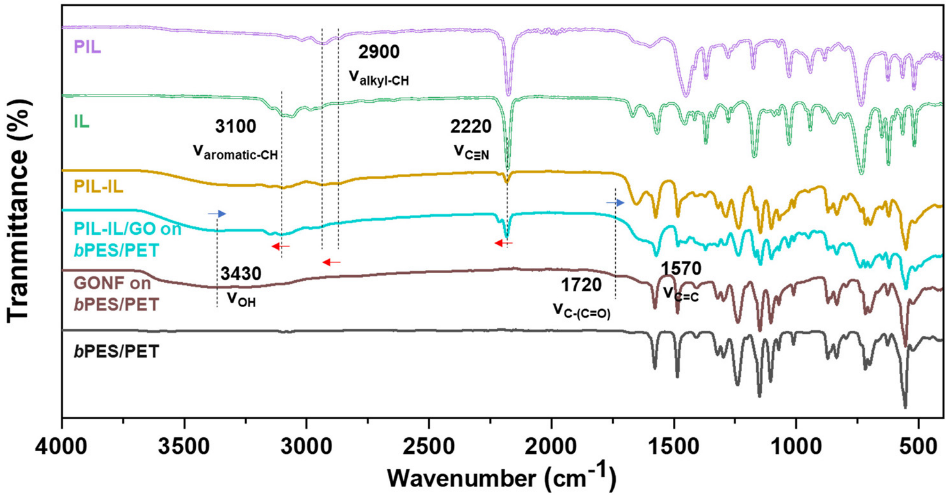

Fig. 5 FTIR spectra of PIL, IL, PIL–IL, PIL–IL/GO on *b*PES/PET, GONF on *b*PES/PET, and *b*PES/PET substrate. The vertical dashed lines mark the resonance peak of ν_{OH} 3430 cm^{-1} (GONF), $\nu_{aromatic\text{-}CH}$ 3100 cm^{-1} (IL), $\nu_{alkyl\text{-}CH}$ 2900 cm^{-1} (PIL), $\nu_{C\equiv N}$ 2220 cm^{-1} (PIL and IL), $\nu_{C-(C=O)}$ 1720 cm^{-1} (GONF), $\nu_{C=C}$ 1570 cm^{-1} (GONF). The arrows indicate the red and blue shift-direction of each vibration in the PIL–IL/GO, due to molecular interactions among the constituents.

according to the conditions summarized in Table 1. Fig. 7 shows the performance of PIL–IL/GO on *b*PES/PET substrate (ii in Table 1); both with (hollowed symbols) and without O_2 (filled symbols). CO_2 permeance of 3900 GPU (Fig. 7a) and CO_2/N_2 selectivity of 1200 (Fig. 7b) were measured under 410 ppm CO_2 with $CO_2/N_2/H_2O$ mixture feed at 40% RH and

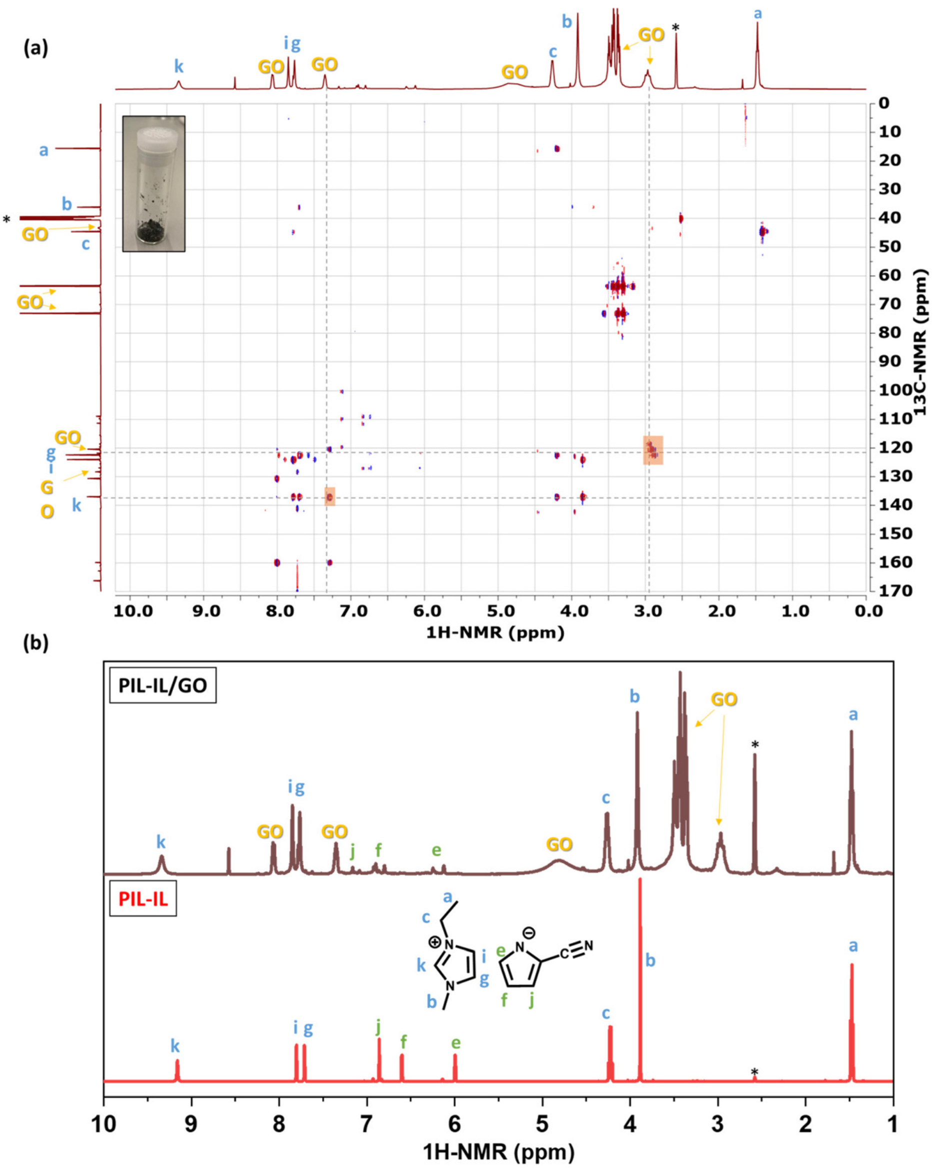

Fig. 6 (a) HMBC spectra showing the molecular interactions between PIL, IL, and GO components. Inset shows the images of PIL–IL/GO material collected by scraping off the top selective layer from the PIL–IL/GO on *b*PES/PET to redisperse in DMSO-d_6 for HMBC NMR. (b) ^{1}H-NMR of the PIL–IL/GO and PIL–IL gel. The GO peaks, from high field to down field, are likely due to the native alkyl-CH (~3 ppm), OH (4.7 ppm), aromatic-CH (~7 ppm) functionalities that are captured due to their interaction with the IL. The NMR of pure GO is shown in Fig. S8.†

22 °C. Under 2500 ppm CO_2 (cabin air), the performance was 1360 GPU with a CO_2/N_2 selectivity of 650. The exponential decrease in CO_2 permeance with increased CO_2 concentration in feed is a characteristic trait of facilitated transport (F-T) mechanism. The permeances for the non-reactive O_2 and N_2 stay constant around 6 GPU for O_2 and 1 GPU for N_2. The F-T pathway dominates over S–D mechanism for CO_2 transport at these low partial pressure conditions. While the CO_2/N_2 selectivity of the FTM with *b*PES/PET substrate (ii in Table 1) was about the same as the one with the UF substrate (i in Table 1; Fig. S9b†), PIL–IL/GO on *b*PES/PET presented 10% higher CO_2 permeance under both DAC and cabin air conditions with $CO_2/N_2/H_2O$ mixture feed (Fig. S9a†). Following the resistance-in-series model, this increase in permeance is ascribed to the thinner *b*PES skin layer with larger pore size (30–40 nm) that is interconnected as opposed to the semi-dense PES layer (pore size 3–4 nm) of the commercial UF substrate.[57,64,69] The CO_2 permeance decreased by about 45% in the presence of O_2 to 2100 GPU at 410 ppm of CO_2 (Fig. 7a). This was observed irrespective of the substrate used (Fig. S9a†). Recalling that the solubility of CO_2 in IL is barely changed with and without the presence of O_2 presence (Fig. 2a), we suggest that the decrease in CO_2 permeance is related with the slower diffusion of CO_2 and CO_2-complexes within the membrane (Fig. 2b). The CO_2/O_2 selectivity (265 at 410 ppm CO_2) is lower than that of CO_2/N_2 selectivity (1100)

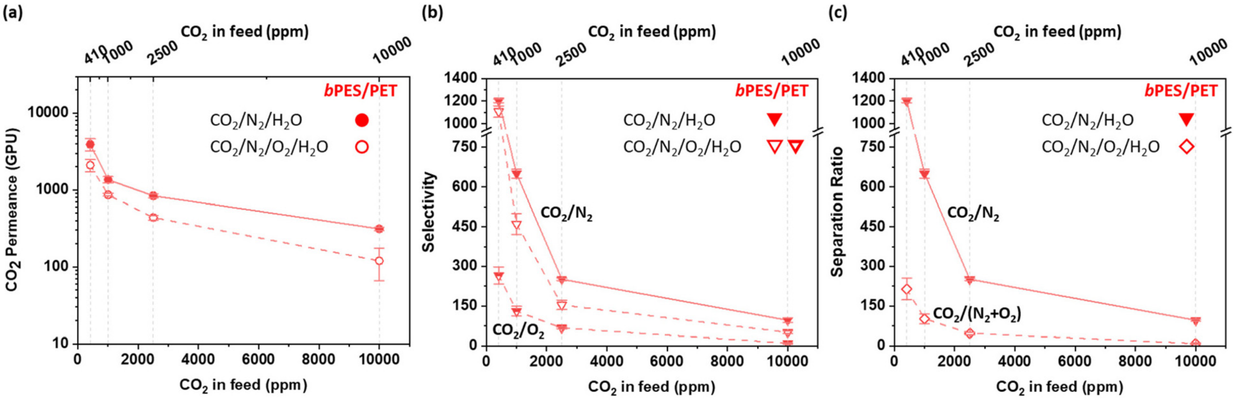

Fig. 7 (a) Permeance of PIL–IL/GO on *b*PES/PET (i in Table 1) under $CO_2/N_2/H_2O$ (filled circle) and $CO_2/N_2/O_2/H_2O$ (hollowed circle). (b) CO_2/N_2 and CO_2/O_2 selectivities. (c) $CO_2/(N_2 + O_2)$ separation ratio. Notice that for $CO_2/N_2/H_2O$ feed, the $CO_2/(N_2 + O_2)$ separation ratio is the same as CO_2/N_2 selectivity. The feed gas had a humidity level of 40% RH at 22 °C; 10.6 mbar moisture.

since O_2 (~5 GPU) is in general more permeable than N_2 (~1.5 GPU), mainly due to their difference in molecular size (O_2: 3.46 Å *vs.* N_2: 3.64 Å). Fig. 7c shows the separation ratio of PIL–IL/GO on *b*PES/PET with and without O_2. The PIL–IL/GO on *b*PES/PET was observed to have lower separation ratio due to the higher permeance of O_2 than N_2.

The experimental data presented in Fig. 7a was fitted to the facilitated transport model (eqn (6)) to extract parameters of $P^0_{CO_2}/l$ and $p^*_{CO_2}$ (Fig. S10†). The $P^0_{CO_2}/l$ parameter (in units of GPU) corresponds to the CO_2 permeance of FTMs at complete carrier saturation and therefore represents the S–D portion of the overall CO_2 permeance. The fitted values of $P^0_{CO_2}/l$ are magnitudes lower than the overall measured CO_2 permeance P_{CO_2}/l; consistent with FTM behavior where CO_2 permeance decreases with increasing CO_2 concentration since the membrane starts to behave more like S–D membrane or even as a membrane absorber at high CO_2 partial pressures. The extracted CO_2 permeance at carrier saturation of the PIL–IL/GO on UF under CO_2/N_2 is 32.6 GPU, which is in the vicinity of the previously reported CO_2 permeance of 19 GPU at higher CO_2 concentration of 15% at 22 °C.[56] Further comparing the extracted value of $p^*_{CO_2}$ (Fig. S10† inset table) under the condition with and without O_2, CO_2 saturation of carriers within the membrane seems more likely to happen when there is O_2 present, regardless of the membrane substrate used. The slower ion-self diffusivity in the presence of O_2 as seen in Fig. 2b also supports this observation.

Factors like humidity[70] and temperature[39] are known to influence the transport behavior in FTMs. Under high humidity, water is co-absorbed with CO_2. The presence of water is known to decrease the viscosity of ILs and it also increases the CO_2 capacity due to the reaction between CO_2 and water that forms bicarbonate.[56] On the other hand, increase in temperature not only increases chain mobility in PIL (hence faster CO_2 transport) but also encourages the dissociation of IL–CO_2 complex (hence faster CO_2 release) due to the exothermic nature of CO_2 absorption. Therefore, CO_2 separation from air for PIL–IL/GO on *b*PES/PET was evaluated at different humidity levels and temperatures as shown in Fig. 8a and b, respectively. The CO_2 permeance, CO_2/N_2 selectivity, and separation ratio all increase with increased humidity and temperature, primarily owing to the faster transport of the CO_2. (See ESI† for more detailed discuss on the temperature effect on FTM performance.) A higher CO_2 transport was achieved with higher moisture content, since humidity not only increases the binding of CO_2 to IL carrier (*via* greater extent of bicarbonate formation) but also increases the diffusivity of the carriers due to lubrication effect from water co-absorption (Fig. S11†). With increased temperature, CO_2 and IL–CO_2 complex diffusivities are expected to increase, so does the dissociation rate of IL–CO_2 complex. There is much discussion in the field[71] on whether it is the increase of the carrier mobility[49] or the CO_2 dissociation rate[47] that dominates for higher CO_2 separation performance with increased temperature. A recent study on high performance FTMs at room temperature suggest the rate determining step is the diffusion.[54] Therefore, not surprisingly the separation performance decayed with increased thickness of selective layer (from ii to iv in Table 1) as seen in Fig. 8c due to the increased film resistance to diffusion. Fig. 8d further demonstrates the stability of PIL–IL/GO on *b*PES/PET over the course of 7 days under continuous feed of 410 ppm CO_2 at 40% RH and 295 K. We believe that the nano-confinement of PIL–IL within GONF (through (1) π–π interaction and (2) electrostatic interactions) played a pivotal role for this stability.[56]

We further tested PIL–IL/GO on *b*PES/PET under vacuum operation with 760 Torr transmembrane pressure. Membranes ii, iii, and iv (in Table 1) leaked. We noticed the transmembrane pressure gradient could not be maintained and the permeate composition was almost the same as the feed, suggesting the need of further mechanical reinforcement on the selective PIL–IL/GO layer. Table S1† shows our efforts of changing the PIL–IL/GO composition by gradually increasing the PIL and GO loading of the selective layer. The increase of PIL and GO components increased the mechanical stability of the PIL–IL/GO; however, this was accompanied with significant reductions in CO_2 binding capacity and transport. The high

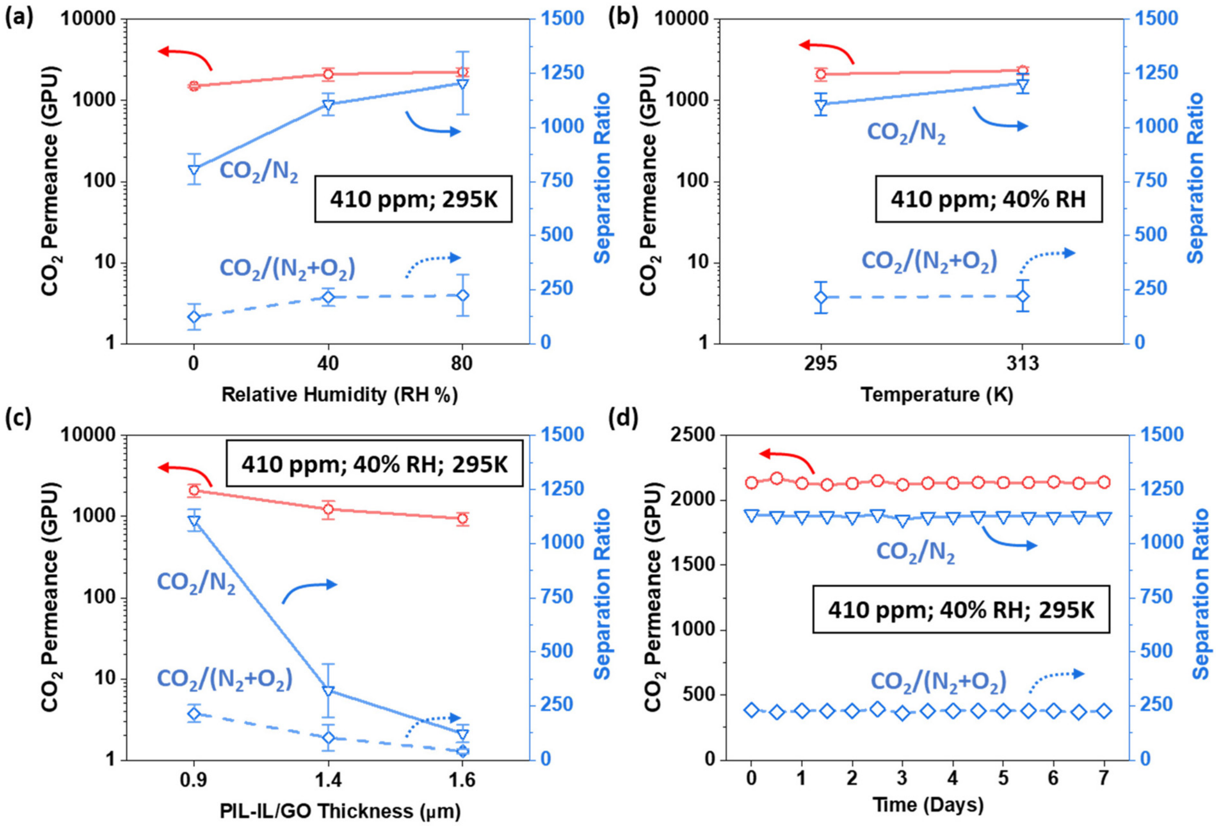

Fig. 8 The change in CO$_2$ separation performance with humidity (a), temperature (b), membrane thickness (c), and time (d). Membrane ii (in Table 1) is used in panel (a), (b), and (d); and membrane ii, iii, and iv are used in panel (c).

content of PIL also led to a relative brittle film (see Fig. 3) where cracks could form even under the plasticization by moisture at 40% RH (*i.e.*, samples 3 and 7 in Table S1†). However, it was demonstrated that a PIL–IL/GO of 1.27–3.75/1 (v in Table 1; sample 21 in Table S1†) withstands the pressure gradient. Fig. 9 shows CO$_2$ separation performance at 295 and 313 K for the FTM sample v. At 295 K, the F-T pathway appears to be more hindered due to the higher PIL content, which is less reactive to CO$_2$ without the imidazolium moiety in the ionomer structure, and the thicker selective layer. The performance resembles an S–D membrane, where a CO$_2$ permeance of 31 GPU and separation ratio of 6.2 were measured. At 313 K, the F-T mechanism was enhanced due to improved diffusivity with increased temperature, the CO$_2$ permeance increased by 15-fold along with an increase in CO$_2$/N$_2$ selectivity. However, the CO$_2$/O$_2$ selectivity remains about the same, possibly due to the enhanced O$_2$ diffusion. These results demonstrate that even a relatively small increase in the thickness of the selective layer for mechanical stability results in dramatic reduction in the FTM performance, thus identifying the mass transport resistance as the most critical factor. Therefore, our recommendation for future research direction for PIL–IL type of FTMs is chemical modifications of the selective layer so that the carriers can be covalently bonded in order to achieve both the superior separation performance and the durability in particular for transmembrane pressures larger than zero.

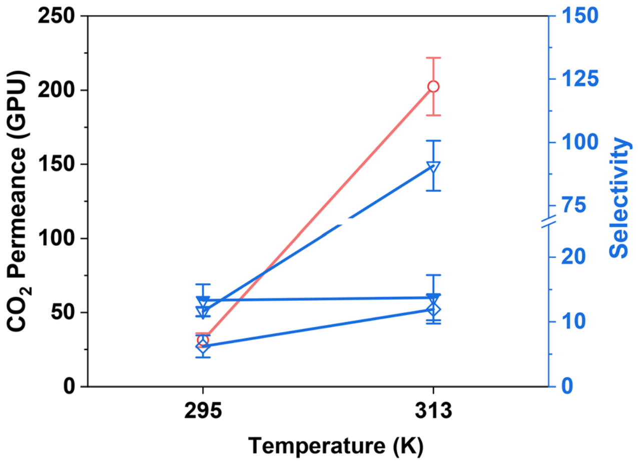

Fig. 9 Performance of vacuum operation of PIL–IL/GO on *b*PES/PET (v in Table 1) under 410 ppm CO$_2$ with mixture feed of CO$_2$/N$_2$/O$_2$ at 22 and 40 °C; both with 40% RH.

Conclusions

An FTM with PIL–IL/GO selective layer was fabricated using a highly permeable bicontinuous structured *b*PES/PET substrate.

The nanoconfinement of PIL–IL within the GONF layer through ionic interactions between the carriers and the GO flakes and π–π interactions between the aromatic moieties was effective in maintaining the membrane stability under zero transmembrane pressure. The presence of O_2 in the feed did not affect the carrier-CO_2 binding capacity under the tested conditions, however it resulted in slightly slower CO_2 transport. The fabricated FTM with PIL–IL/GO selective layer and the *b*PES/PET substrate presented a CO_2 permeance of 2100 GPU and high selectivities of CO_2/N_2 (1100) and CO_2/O_2 (265) under conditions relevant to DAC (410 ppm CO_2, 40% RH, 295 K). Under 2500 ppm of CO_2, conditions relevant to cabin air, the permeance decreases to 430 GPU while the CO_2/N_2 selectivity and CO_2/O_2 selectivity dropped to 150 and 67, respectively. These results demonstrate a superior performance, especially the CO_2/O_2 selectivity, among the known FTMs reported to date. Further, this study represents the first FTM for CO_2 separation from air. To improve the membrane stability and to prevent leaching of the carrier for operations under a positive transmembrane pressure, the selective layer thickness was increased. The thicker membranes presented significant resistance thus resulting in lower separation performance. In order to further tune the membrane stability without increasing the thickness and resistance, covalent interactions between the PIL–IL and GO within a thin selective layer are determined to be necessary.

Author contributions

Y. Y. L. synthesized the IL and PIL, and fabricated, characterized, and tested the membranes. N. P. W. assisted in performing the DOSY and HMBC NMR measurements. R. D. measured CO_2 capacities. D. L. J. contributed to the experimental plans and the discussions on the CO_2 removal from cabin air. B. G. oversaw the experiments and analysis. All authors contributed to the writing of the manuscript.

Conflicts of interest

There are no conflicts to declare.

Acknowledgements

This work was supported by an Early Career Faculty grant from NASA's Space Technology Research Grants Program under Award No. 80NSSC18K1505. The characterization of IL–CO_2 binding and self-diffusivity under DAC relevant conditions were supported by the U.S. Department of Energy, Office of Science, Basic Energy Science under award Number DE-SC0022214. The authors would like to thank Dr Ruizhi Pang and Dr W. S. Winston Ho for providing the *b*PES/PET substrate. The authors acknowledge the Northeast Ohio High Field NMR Facility, Swagelok Center for Surface Analysis of Materials (SCSAM) for the access to SEM, and the Soft Matter Characterization Laboratory for the access to TGA at Case Western Reserve University.

References

1 J. C. Knox, 47th Int. Conf. Environ. Syst., 2017, ICES-2017-209.

2 R. Huang, J. T.-M. Richardson, G. Belancik and D. Jan, 47th Int. Conf. Environ. Syst., 2017, ICES-2017-116.

3 D. G. Madden, H. S. Scott, A. Kumar, K. Chen, R. Sanii, A. Bajpai, M. Lusi, T. Curtin, J. J. Perry, M. J. Zaworotko and T. Curtin, *Philos. Trans. R. Soc., A*, 2017, **375**, 2084–2094.

4 J. C. Knox, 48th Int. Conf. Environ. Syst., 2018, ICES-2018-215.

5 Overview of Greenhouse Gases, https://www.epa.gov/ghgemissions/overview-greenhouse-gases.

6 National Academies, *Negative Emissions Technologies and Reliable Sequestration: A Research Agenda*, 2019.

7 K. Z. House, A. C. Baclig, M. Ranjan, E. A. Van Nierop, J. Wilcox and H. J. Herzog, *Proc. Natl. Acad. Sci. U. S. A.*, 2011, **108**, 20428–20433.

8 R. P. Lively and M. J. Realff, *AIChE J.*, 2016, **62**, 3699–3705.

9 M. V. Paragano and J. Kolmas, 45th Int. Conf. Environ. Syst., 2015, ICES-2015-112.

10 F. Zeman, *Environ. Sci. Technol.*, 2007, **41**, 7558–7563.

11 M. Erans, E. S. Sanz-Pérez, D. P. Hanak, Z. Clulow, D. M. Reiner and G. A. Mutch, *Energy Environ. Sci.*, 2022, **15**, 1360–1405.

12 R. Custelcean, N. J. Williams, K. A. Garrabrant, P. Agullo, F. M. Brethomé, H. J. Martin and M. K. Kidder, *Ind. Eng. Chem. Res.*, 2019, **58**, 23338–23346.

13 J. K. Stolaroff, D. W. Keith and G. V. Lowry, *Environ. Sci. Technol.*, 2008, **42**, 2728–2735.

14 K. Lackner, H.-J. Ziock and P. Grimes, in Conference: 24th Annual Technical Conference on Coal Utilization and Fuel Systems, Clearwater, FL (US), Clearwater, Florida, 1999.

15 A. Holewinski, M. A. Sakwa-Novak and C. W. Jones, *J. Am. Chem. Soc.*, 2015, **137**, 11749–11759.

16 A. R. Sujan, S. H. Pang, G. Zhu, C. W. Jones and R. P. Lively, *ACS Sustainable Chem. Eng.*, 2019, **7**, 5264–5273.

17 S. Bali, M. A. Sakwa-Novak and C. W. Jones, *Colloids Surf., A*, 2015, **486**, 78–85.

18 T. Wang, K. S. Lackner and A. Wright, *Environ. Sci. Technol.*, 2011, **45**, 6670–6675.

19 X. Shi, H. Xiao, H. Azarabadi, J. Song, X. Wu, X. Chen and K. S. Lackner, *Angew. Chem., Int. Ed.*, 2020, **59**, 6984–7006.

20 E. A. Van Nierop, S. Hormoz, K. Z. House and M. J. Aziz, *Energy Procedia*, 2011, **4**, 1783–1790.

21 Y. Duan and D. C. Sorescu, *J. Chem. Phys.*, 2010, **133**, 1–11.

22 S. T. Hwang, *AIChE J.*, 2004, **50**, 862–870.

23 H. B. Park, J. Kamcev, L. M. Robeson, M. Elimelech and B. D. Freeman, *Science*, 2017, **356**, 1138–1148.

24 W. J. Koros and C. Zhang, *Nat. Mater.*, 2017, **16**, 289–297.

25 I. Kammakakam, K. E. O'Harra, E. M. Jackson and J. E. Bara, *Polymer*, 2021, **214**, 123239.

26 A. R. Nabais, R. O. Francisco, V. D. Alves, L. A. Neves and L. C. Tomé, *Membranes*, 2021, **11**, 1–19.

27 I. Kammakakam, J. E. Bara, E. M. Jackson, J. Lertxundi, D. Mecerreyes and L. C. Tomé, *ACS Sustainable Chem. Eng.*, 2020, **8**, 5954–5965.

28 J. Liu, S. Zhang, D. e. Jiang, C. M. Doherty, A. J. Hill, C. Cheng, H. B. Park and H. Lin, *Joule*, 2019, **3**, 1881–1894.

29 S. Tachibana, K. Hashimoto, H. Mizuno, K. Ueno and M. Watanabe, *Polymer*, 2022, **241**, 124533.

30 Z. Huang, C. Yin, T. Corrado, S. Li, Q. Zhang and R. Guo, *Chem. Mater.*, 2022, **34**, 2730–2742.

31 T. J. Corrado, Z. Huang, D. Huang, N. Wamble, T. Luo and R. Guo, *Proc. Natl. Acad. Sci. U. S. A.*, 2021, **118**, 1–7.

32 J. G. Seong, W. H. Lee, J. Lee, S. Y. Lee, Y. S. Do, J. Y. Bae, S. J. Moon, C. H. Park, H. J. Jo, J. S. Kim, K. R. Lee, W. S. Hung, J. Y. Lai, Y. Ren, C. J. Roos, R. P. Lively and Y. M. Lee, *Sci. Adv.*, 2021, **7**, 1–11.

33 I. Rose, C. G. Bezzu, M. Carta, B. Comesanã-Gándara, E. Lasseuguette, M. C. Ferrari, P. Bernardo, G. Clarizia, A. Fuoco, J. C. Jansen, K. E. Hart, T. P. Liyana-Arachchi, C. M. Colina and N. B. McKeown, *Nat. Mater.*, 2017, **16**, 932–937.

34 L. Hu, V. T. Bui, A. Krishnamurthy, S. Fan, W. Guo, S. Pal, X. Chen, G. Zhang, Y. Ding, R. P. Singh, M. Lupion and H. Lin, *Sci. Adv.*, 2022, **8**, 27–29.

35 B. Comesaña-Gándara, J. Chen, C. G. Bezzu, M. Carta, I. Rose, M. C. Ferrari, E. Esposito, A. Fuoco, J. C. Jansen and N. B. McKeown, *Energy Environ. Sci.*, 2019, **12**, 2733–2740.

36 B. W. Rowe, L. M. Robeson, B. D. Freeman and D. R. Paul, *J. Membr. Sci.*, 2010, **360**, 58–69.

37 L. M. Robeson, *J. Membr. Sci.*, 2008, **320**, 390–400.

38 A. Klemm, Y. Y. Lee, H. Mao and B. Gurkan, *Front. Chem.*, 2020, **8**, 1–8.

39 Y. Han and W. S. W. Ho, *Ind. Eng. Chem. Res.*, 2020, **59**, 5340–5350.

40 E. Kamio, M. Tanaka, Y. Shirono, Y. Keun, F. Moghadam, T. Yoshioka, K. Nakagawa and H. Matsuyama, *Ind. Eng. Chem. Res.*, 2020, **59**, 2083–2092.

41 Y. Han, D. Wu and W. S. W. Ho, *J. Membr. Sci.*, 2018, **567**, 261–271.

42 S. Zhang, H. Li, H. Li, B. Sengupta, S. Zha, S. Li and M. Yu, *Adv. Funct. Mater.*, 2020, **30**, 2002804.

43 S. Janakiram, F. Santinelli, R. Costi, A. Lindbråthen, G. M. Nardelli, K. Milkowski, L. Ansaloni and L. Deng, *Chem. Eng. J.*, 2021, **413**, 127405.

44 S. Janakiram, J. L. Martín Espejo, X. Yu, L. Ansaloni and L. Deng, *J. Membr. Sci.*, 2020, **616**, 118626.

45 J. Zhang, E. Kamio, A. Matsuoka, K. Nakagawa, T. Yoshioka and H. Matsuyama, *Ind. Eng. Chem. Res.*, 2021, **60**, 12640–12649.

46 J. Zhang, E. Kamio, M. Kinoshita, A. Matsuoka, K. Nakagawa, T. Yoshioka and H. Matsuyama, *Ind. Eng. Chem. Res.*, 2021, **60**, 12698–12708.

47 Y. Han and W. S. W. Ho, *J. Membr. Sci. Lett.*, 2022, **2**, 100014.

48 X. Deng, C. Zou, Y. Han, L.-C. Lin and W. S. W. Ho, *J. Phys. Chem. C*, 2020, **124**, 25322–25330.

49 A. Matsuoka, S. Taniguchi, E. Kamio and H. Matsuyama, *Ind. Eng. Chem. Res.*, 2021, **60**, 7397–7405.

50 D. T. Wickham, K. J. Gleason, J. R. Engel, S. W. Cowley and C. Chullen, *43th Int. Conf. Environ. Syst.*, 2013, 1–18.

51 D. T. Wickham, J. A. Nabity, J. McCarty and R. Aaron, *49th Int. Conf. Environ. Syst.*, 2019, ICES-2019-187.

52 S. Fujikawa, R. Selyanchyn and T. Kunitake, *Polym. J.*, 2021, **53**, 111–119.

53 C. Castel, R. Bounaceur and E. Favre, *Front. Chem. Eng.*, 2021, **3**, 1–15.

54 M. Sandru, E. M. Sandru, W. F. Ingram, J. Deng, P. M. Stenstad, L. Deng and R. J. Spontak, *Science*, 2022, **376**, 90–94.

55 B. Belaissaoui, E. Lasseuguette, S. Janakiram, L. Deng and M. C. Ferrari, *Membranes*, 2020, **10**, 1–23.

56 Y. Y. Lee and B. Gurkan, *J. Membr. Sci.*, 2021, **638**, 119652.

57 R. Pang, K. K. Chen, Y. Han and W. S. W. Ho, *J. Membr. Sci.*, 2020, **612**, 118443.

58 Y. Y. Lee, D. Penley, A. Klemm, W. Dean and B. Gurkan, *ACS Sustainable Chem. Eng.*, 2021, **9**, 1090–1098.

59 Y. Y. Lee, K. Edgehouse, A. Klemm, H. Mao, E. Pentzer and B. Gurkan, *ACS Appl. Mater. Interfaces*, 2020, **12**, 19184–19193.

60 N. A. Ramli, N. A. Hashim and M. K. Aroua, *Chem. Eng. Commun.*, 2018, **205**, 295–310.

61 H. Tokuda, K. Hayamizu, K. Ishii, M. A. B. H. Susan and M. Watanabe, *J. Phys. Chem. B*, 2004, **108**, 16593–16600.

62 S. M. Green, M. E. Ries, J. Moffat and T. Budtova, *Sci. Rep.*, 2017, **7**, 1–12.

63 A. Radhi, K. A. Le, M. E. Ries and T. Budtova, *J. Phys. Chem. B*, 2015, **119**, 1633–1640.

64 R. Pang, Y. Yang, Y. Han, K. K. Chen and W. S. W. Ho, *J. Membr. Sci.*, 2022, **654**, 120547.

65 W. Ying, J. Cai, K. Zhou, D. Chen, Y. Ying, Y. Guo, X. Kong, Z. Xu and X. Peng, *ACS Nano*, 2018, **12**, 5385–5393.

66 X. Wan, K. Zhang, T. Wan, Y. Yan, Z. Ye and X. Peng, *J. Membr. Sci.*, 2022, **652**, 120475.

67 M. Dong, K. Zhang, X. Wan, S. Wang, S. Fan, Z. Ye, Y. Wang, Y. Yan and X. Peng, *Small*, 2022, **18**, 2108026.

68 M. Dong, K. Zhang, X. Wan, Z. Fang, Y. Hu, Z. Ye, Y. Wang, Z. Li and X. Peng, *Appl. Mater. Today*, 2022, **27**, 101458.

69 R. Pang, Y. Han, K. K. Chen, Y. Yang and W. S. W. Ho, *Appl. Energy*, 2022, **311**, 118624.

70 X. Deng, Y. Han, L. C. Lin and W. S. W. Ho, *J. Phys. Chem. C*, 2022, **126**, 3661–3670.

71 A. Matsuoka, A. Otani, E. Kamio and H. Matsuyama, *Sep. Purif. Technol.*, 2022, **280**, 119847.